RADIATION HARDNESS OF THE PIBETA DETECTOR COMPONENTS

E. FRLEŽ, T. A. CAMPBELL, I. J. CAREY and D. POČANIĆ

Department of Physics, University of Virginia, Charlottesville, VA 22904-4714, USA

Paper devoted to honour the memory of Professor Nikola Cindro

We have examined long-term changes in signal amplitude gain, energy resolution and detection efficiency of the active components of the PIBETA detector system. Beam-defining plastic scintillation counters were operated in a $\sim 1\,\mathrm{MHz}$ stopped π^+ beam for a period of 297 days, accumulating radiation doses of up to $2 \cdot 10^6$ rad. Detectors in the charged particle tracking system — a pair of cylindrical multi-wire proportional chambers and a thin plastic scintillation barrel-shaped hodoscope array — were irradiated during the same running period with an average dose of $\sim 4 \cdot 10^4$ rad. Individual CsI (undoped crystal) calorimeter detectors received an average dose of ~ 120 rad, mainly from photons, positrons and protons originating from π^+ hadronic interactions as well as from π^+ and μ^+ weak decays at rest in the active target.

1. Introduction

The PIBETA collaboration has proposed a program of precise measurements of rare π and μ decays at the Paul Scherrer Institute (PSI) [1], with particular emphasis on the pion beta decay branching ratio, $\Gamma(\pi^+ \to \pi^0 e^+ \nu_e)$.

The PIBETA apparatus is a large solid angle non-magnetic detector optimized for detection of photons and electrons in the energy range of $5 - 150\,\mathrm{MeV}$ with high efficiency, energy resolution and solid angle. The main sensitive components of the apparatus, shown and labeled in Fig. 1, are:
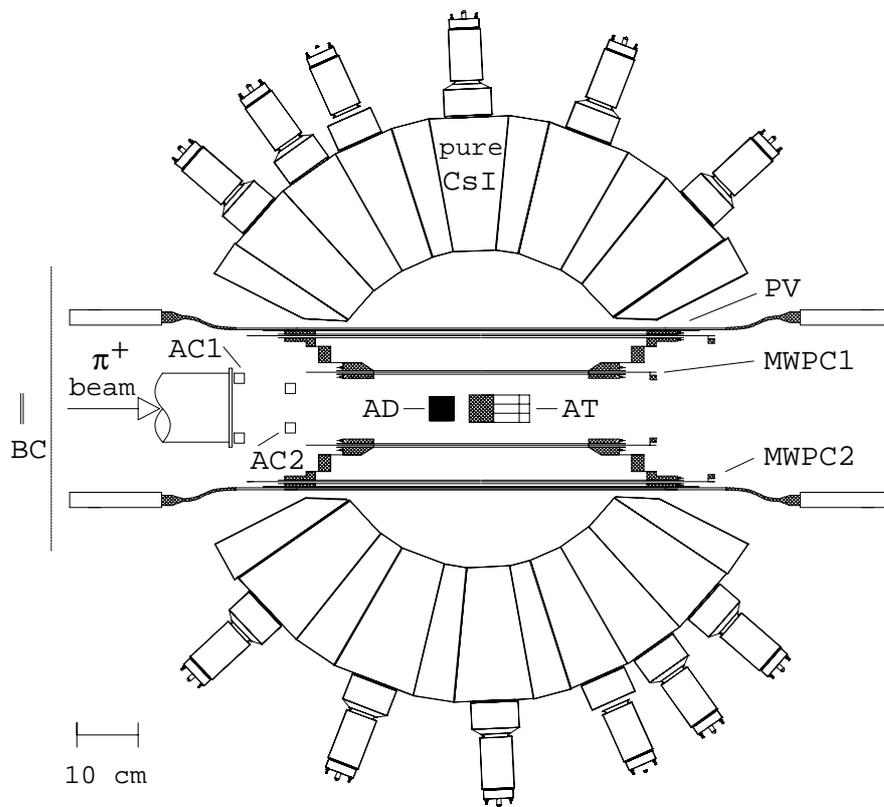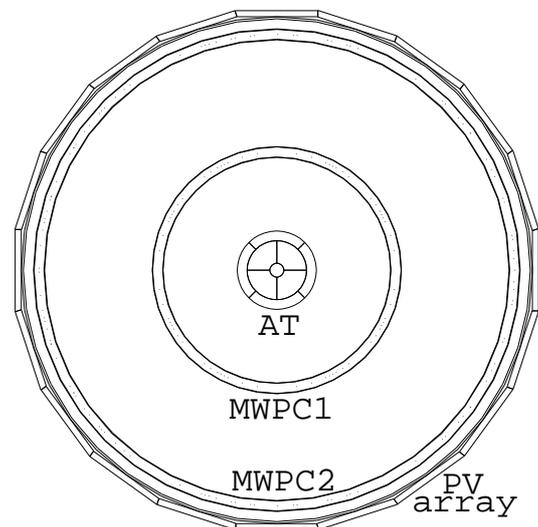
Fig. 1. (above) Schematic cross section of the PIBETA apparatus showing the main components: beam entry counters (BC, AC1, AC2), active degrader (AD), active target (AT), wire chambers (MWPCs) and support, plastic veto (PV) detectors and PMTs, pure CsI calorimeter and PMTs. (right) Axial (beam) view of the central detector region showing the 9-element active target and the charged particle tracking detectors.

(1) a thin forward beam counter placed approximately 4 m upstream of the detector center (BC), two cylindrical active collimators (AC$_1$ and AC$_2$), an active degrader (AD), all made of plastic scintillator and used for beam definition;

(2) a 9-element segmented active plastic scintillator target (AT), used to stop the beam particles while simultaneously sampling the lateral beam profile;

(3) two concentric low-mass cylindrical multi-wire proportional chambers for charged particle tracking (MWPC$_1$ and MWPC$_2$), surrounding the active target;

(4) a fast 20-bar segmented thin plastic scintillator hodoscope (PV), surrounding the MWPCs, used for particle identification;

(5) a 240-element fast high-resolution segmented spherical pure-CsI shower calorimeter surrounding the target region and tracking detectors, subtending a solid angle of about 80% of 4π;

(6) a set of cosmic muon plastic scintillator veto counters (CV) around the entire apparatus, not shown in Fig. 1.

The detector components listed above, together with delay cables for photomultiplier tube (PMT) analog signals, high voltage (HV) supplies and cables, MWPC instrumentation and gas system, fast trigger electronics, two front end computers (one for data acquisition, the other for slow control), as well as the temperature control system, are all mounted on a single platform that is moved as a single unit in and out of the experimental area. Thus, the detector can become fully operational in less than 24 hours after the support platform is precisely positioned with respect to the beam line, and electrical power and Ethernet connections are made.

The building and testing of the detector components were completed in 1998, followed by the assembly and commissioning of the full detector apparatus. Data acquisition with the PIBETA detector started in the second half of 1999, initially at a reduced pion stopping rate, as planned. Since then, the pion stopping rate was gradually increased and the experiment ran during most of the available beam period in the years 2000 and 2001 at about 1 MHz π^+ stopping rate.

In all important respects, the detector has met its design specifications. In this paper, we report on the radiation resistance and the temporal stability of the gain, energy resolution and detection efficiency of the most affected active elements of the PIBETA detector listed above.

Radiation stability of the plastic scintillator detectors used in high energy and nuclear physics experiments is one of their main characteristics, and as such has been discussed in a voluminous body of research and review papers. Here we note a review paper by G. Marini et al. [2] and Refs. [3–8], as well as references therein. These papers address the issue of experimentally determining and improving the radiation hardness of plastic scintillators.

Radiation hardness of pure (undoped) CsI scintillators has been reported in Refs. [9–13].

2. Experimental analysis

The PIBETA measurements are performed in the $\pi E1$ channel at PSI [14]. For this experiment, the beam line is operated in the high-intensity, low-momentum resolution mode. Correspondingly, a 114 MeV/c π^+ beam tune has been developed with momentum spread of $\Delta p/p \leq 1.2\%$ and maximum nominal π^+ beam intensity of $I_\pi \simeq 2 \cdot 10^6 \, \pi^+/\mathrm{s}$.

The spatial spread of the π^+ beam is restricted by a 10 cm thick lead collimator with a 7 mm diam. pin-hole located 3985 mm upstream of the detector center. Beam particles are first registered in the 2 mm thick plastic scintillator (BC) placed directly downstream of the collimator. Pions are subsequently slowed down in the 40 mm long active plastic degrader (AD), and stopped in the active plastic target (AT) positioned in the center of the PIBETA detector, Fig. 1.

We have analyzed a total of 6213 production runs, for which data were accumulated between 9 October 1999 and 11 December 2000. This data set comprises a total number of $1.4 \cdot 10^{13}$ beam π^+'s stopped in the active target. The e^+ and μ^+ beam contaminations measured in the BC–AT time-of-flight spectrum are small, $\approx 0.4\%$ and $\approx 0.2\%$, respectively. Therefore, the in-beam detectors were exposed primarily to pions, while the AT counters also received significant doses from the stopped pion-decay products: $\pi \rightarrow \mu \rightarrow e$. Particle discrimination between the positrons, photons and protons detected in the CsI calorimeter is accomplished using the charged-particle tracking-detector components, i.e., $\mathrm{MWPC}_{1,2}$ and PV, the plastic veto hodoscope.

All individual detector PMT analog signals are discriminated in time-over-threshold CAMAC modules and counted with CAMAC scaler units read out every 10 s. The cumulative scaler counts are updated at the end of every production run in the online database, as well as saved in a computer disk file.

The most probable, as well as the average, energies deposited in each detector element are calculated in a Monte Carlo (MC) simulation using the standard detector description code GEANT3 [15]. The GEANT simulation also provided the average values of radiation exposure throughout the detectors' volumes.

The total energy absorbed per unit detector mass exposed to radiation comprises the received radiation dose. The absorbed radiation dose for each detector is commonly expressed in units of rad [16], corresponding to the energy absorption of 100 erg/g. The equivalent SI unit is 1 Gray equaling 100 rad (1 Gy = 1 Joule/kg). The absorbed radiation doses for each PIBETA active detector element are calculated using the experimental and MC data on ionizing particle types, cumulative particle rates and exposed detector volumes. The PIBETA detector absorbed doses are listed in Tables 1 and 2.

The absolute energy calibration as well as the shapes of experimental deposited energy (ADC) spectra are well understood in the MC GEANT simulations. The peaks in the ADC spectra accumulated for each series of 10 runs are fitted with Gaussian functions in off-line analysis. The means of the Gaussian functions determine the relative detector gain factors, while the standard deviations of the lower parts of the ADC spectra loosely reflect the detector energy resolutions.

TABLE 1. Summary of long-term changes in the gain factors and fractional energy resolution of selected active elements of the PIBETA Detector. 'PVeto' and 'Calo' give the appropriately averaged performance of all PV and CsI elements, respectively.

Detector	Radiation dose (krads)	Initial gain	Final gain	Initial res. (%)	Final res. (%)
BC	2000	1.00	0.66	13.1	13.9
AD	1400	1.00	0.75	7.8	8.5
AT_0	560	1.00	0.76	7.2	10.8
AT_1	630	1.00	0.89	8.4	8.6
AT_5	150	1.00	0.74	7.7	8.9
PV_0	44	1.00	0.99	31.5	32.1
PV_1	40	1.00	0.99	27.6	30.4
PVeto	41	1.00	0.95	26.2	27.9
CsI_0	0.046	1.00	0.89	5.1	5.5
CsI_2	0.045	1.00	0.92	4.9	5.2
CsI_{11}	0.117	1.00	1.02	6.0	6.1
CsI_{19}	0.093	1.00	0.65	5.0	5.3
CsI_{102}	0.152	1.00	0.86	6.0	6.5
CsI_{165}	0.126	1.00	0.74	5.4	5.8
Calo	0.119	1.00	0.83	5.5	6.0

TABLE 2. Summary of long-term changes in the MWPC and PV hodoscope charged particle detection efficiencies.

Detector	Radiation dose (krads)	Initial eff. (%)	Final eff. (%)
$MWPC_1$	41	95.0	95.3
$MWPC_2$	41	98.8	98.1
PVeto	41	99.1	98.9

The PMT bias high voltages were in general kept constant, except for the CsI calorimeter PMTs. The demand HV values were set in 1 V steps with an accuracy and reproducibility of ≈ 1 V, which corresponds to an equivalent gain change of $< 0.5\%$. For the 220 non-peripheral CsI calorimeter detectors, high voltages were adjusted automatically by the on-line analysis computer program on a daily basis. Firm constraints were imposed on the location of the $\pi \rightarrow e\nu$ energy peaks. They

were always forced to the normalized 67.8 MeV value by changing the PMT high voltages and adjusting the calorimeter software gains appropriately.

For a detector equipped with an n-stage PMT operating in the linear domain, a normalized real gain change g, relating two different settings 1 and 2 (at time t_1 and t_2, respectively), depends on the ratio of the software gains s_i and the corresponding high voltages HV_i:

$$g = \frac{s_1}{s_2} \cdot \left(\frac{HV_1}{HV_2} \right)^n .$$

(1)

This equation relates the true gain of a scintillator detector at time t_2 to its gain at time t_1.

3. Plastic-scintillator beam counters

3.1. Forward beam counter (BC)

The forward beam counter BC is the first detector placed right after the beam-defining lead collimator. This counter tags the beam particles that have passed through the collimator.

The central part of the beam counter is a quadratic piece of BICRON BC-400 plastic scintillator [17] with dimensions 25 mm × 25 mm × 2 mm. The scintillator is optically coupled on all four sides to four tapered acrylic lightguides. One lightguide is glued to the scintillator edge surface with BICRON BC-600 optical cement. The other three lightguides have an air gap coupling to the scintillator.

Both the scintillator and the lightguides are mounted inside a light-tight enclosure. This detector-carrying box consists of an aluminum frame with outer dimensions 150 mm × 150 mm × 50 mm, covered by two thin aluminum windows, each 30 μm thick. The Al frame is attached to the lead collimator and keeps the counter position fixed. Feedthroughs at the four lateral sides of the box hold the light guides and the magnetic shield cylinders of the PMTs. The box is, therefore, also used as a mount for the photomultipliers, while keeping the scintillator counter light-tight and protecting it mechanically.

Each of the four lightguides is air-gap coupled to a Hamamatsu R7400U mini-PM tube. The stabilized active PMT voltage divider was specially designed at the University of Virginia for high-rate operation, because the typical counter rates are higher than 2 MHz. The four analog PMT signals are electronically summed in a NIM LCR 428F linear Fan-in/Fan-out unit set up in the experimental beam area.

The analog pulses from the beam counter are divided by a custom-made passive splitter into two signals of equal amplitude. One signal is discriminated in a CAMAC discriminator module; discriminator output is digitized in a FASTBUS Time-to-Digital Converter (TDC) as well as counted with a CAMAC scaler unit. The second signal is connected to a FASTBUS Analog-to-Digital Converter (ADC),

gated with a 100 ns event trigger gate. Similar electronic logic is used with other individual PIBETA detectors discussed in the following sections.

In order to suppress the background caused by detector hits not associated with a π-stop event, we use two active beam collimators AC_1 and AC_2. Both collimators are ring-shaped and are made of a 25.4 mm thick BICRON BC-400 plastic scintillator. AC_1, the first (upstream) ring counter, has an outer diameter of 120 mm and an inner diameter of 50 mm. AC_2, closer to the detector center, has the outer/inner diameter of 172/90 mm, respectively. These dimensions were chosen such that the detectors subtend the various beam tube elements and mechanical support parts of the detector without intersecting the calculated envelope of the beam.

The deposited energy (ADC signal charge) spectrum of the forward beam counter recorded with the π-in-beam trigger is shown in Fig. 2. Most probable energy deposition by a π^+ beam particle corresponds to 0.70 MeV, while the average absorbed energy is 0.80 MeV. These values are calculated with a GEANT Monte Carlo code using a 114 MeV/c π^+ beam as an input. The slope of the low-energy ridge of the deposited energy spectrum in BC is determined by a convolution of the Vavilov probability distribution and the PMT photoelectron statistics. Since the latter deteriorates with radiation damage, the slope of the low-energy edge of the ADC spectrum can be used as a rough indicator of the effects of radiation damage on detector resolution, in the absence of a sharp monoenergetic line. We have used the same approach for the other PIBETA plastic scintillator detectors discussed below, AD, AT and PV.
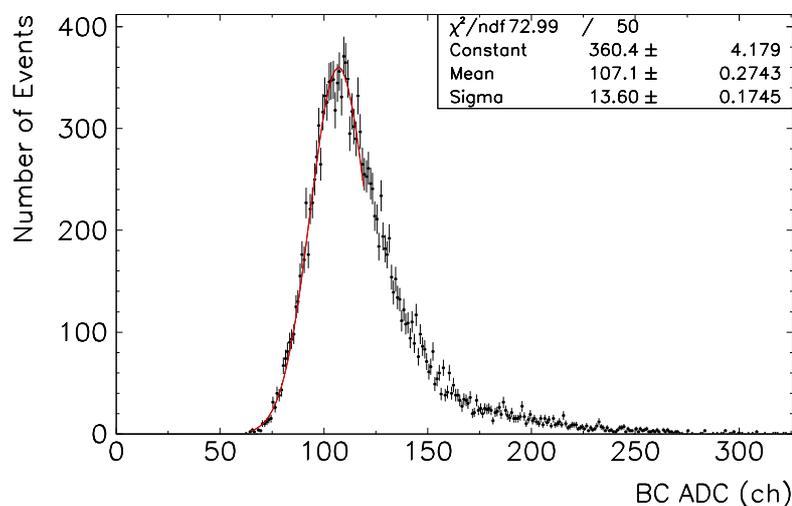

Fig. 2. Energy deposition (ADC signal charge) spectrum of 114 MeV/c π^+'s in BC, the thin forward beam counter. Gaussian fit parameters for the lower energy part of the peak are showed in the statistics window.

Figure 3 depicts the changes in the BC detector gain and fractional energy resolution as the detector became damaged by radiation over time. It is evident from Fig. 3 that the gain of the BC counter decreased approximately linearly over the period of one calendar year due to the radiation exposure of 2 Mrad. The decrease in gain was $\simeq 20\%$/Mrad. The fractional energy resolution for through-going pions was also slightly degraded, changing from 13.1% to 13.9%, as shown in the bottom panel of Fig. 3. Two beam breaks in the radiation exposure, totaling 98 days and 35 days, respectively, resulted in a partial beam counter recuperation and gain increases of $\simeq 10 - 15\%$. The annealing effect on the counter resolution is smaller, though still measurable.
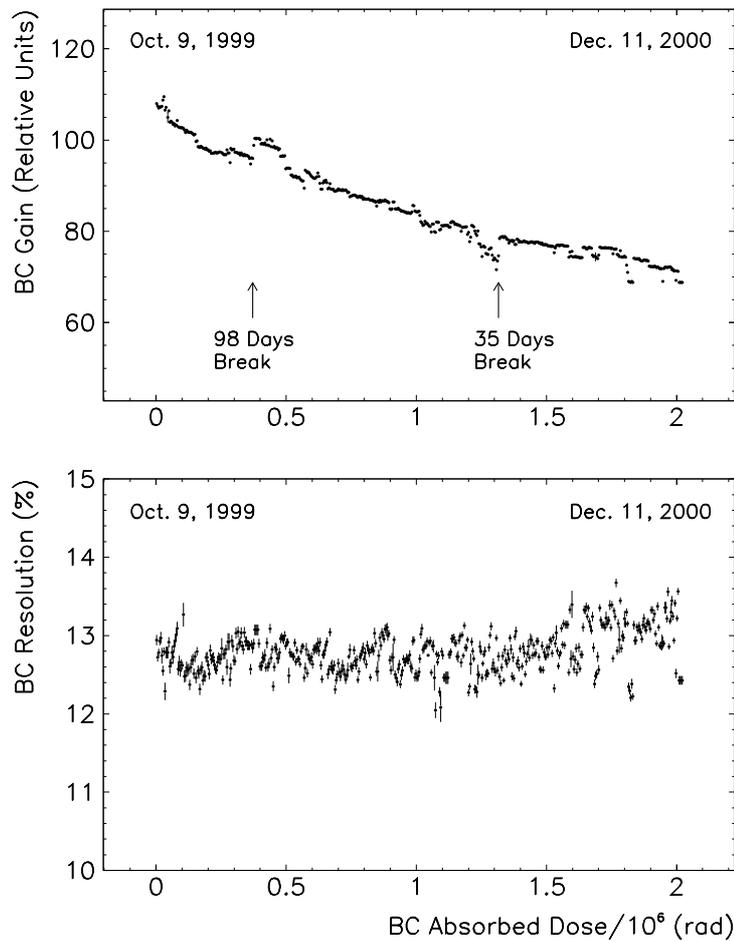

Fig. 3. *Top panel: the change in gain of BC, the forward beam counter, as a function of the absorbed radiation dose in* Mrad. *Bottom panel: fractional energy resolution of the BC detector as a function of the cumulative radiation dose in* Mrad.

3.2. Active Degrader (AD)

The active degrader counter is made of BICRON BC-400 plastic scintillating material in the shape of a cup whose axis is aligned with the beam. The AD fits inside $MWPC_1$ which has an inner clearance of 90 mm diam. The AD outer surfaces are slanted and connect to four acrylic lightguides. This geometry brings the PMTs out of the inner region, at the same time ensuring that the active part of AD (cup "bottom") covers the whole target area (40 mm diameter). The angle and wall thickness of the outer part of the AD are chosen such that a particle traveling parallel to the beam axis transverses the same thickness of 30 mm. The angle is kept small in order to improve light collection efficiency. Each of the four fishtail lightguides ends in a rectangular cross section of 6 mm × 6 mm, which matches the round window area of the Hamamatsu R7400U PMT. The tubes are mounted with an air gap coupling. The four AD PMT analog signals are summed in a NIM LCR 428F linear Fan-in/fan-out unit.
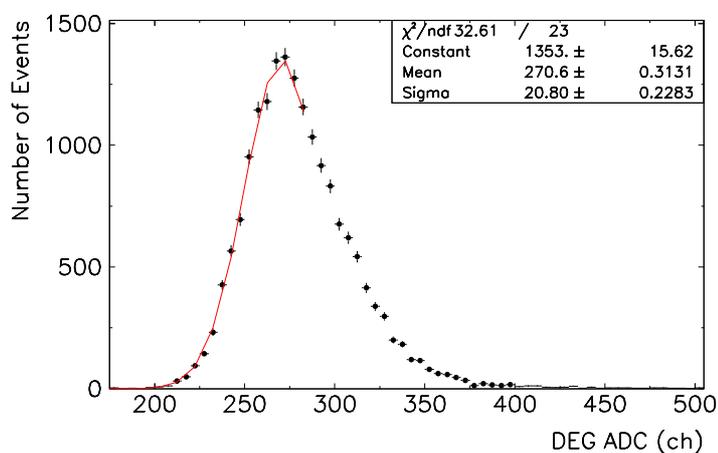

Fig. 4. ADC charge spectrum of the moderated π^+'s in the AD counter. A Gaussian fit (solid curve) is superimposed on the data histogram (points).

The deposited energy (ADC charge) spectrum of the active degrader counter taken with the π-in-beam trigger is shown in Fig. 4. The lower energy part of the deposited energy spectrum is again fitted well with a Gaussian function. Most probable energy deposition of the 114 MeV/c incident π^+ beam is calculated with the GEANT code to be equal to 13.0 MeV, while the average energy absorbed is 13.8 MeV. During the period under analysis, the degrader counter was irradiated with a dose of 1.4 Mrad. The changes in the relative counter gain and energy resolution are shown in the two panels of Fig. 5. Both variables are subject to short-term variations, mostly due to changes in the beam tune. There is, however, an average linear trend in the scintillator gain factor corresponding to 15%/Mrad decrease. The temporal degradation in the AD energy resolution is much smaller but still noticeable.
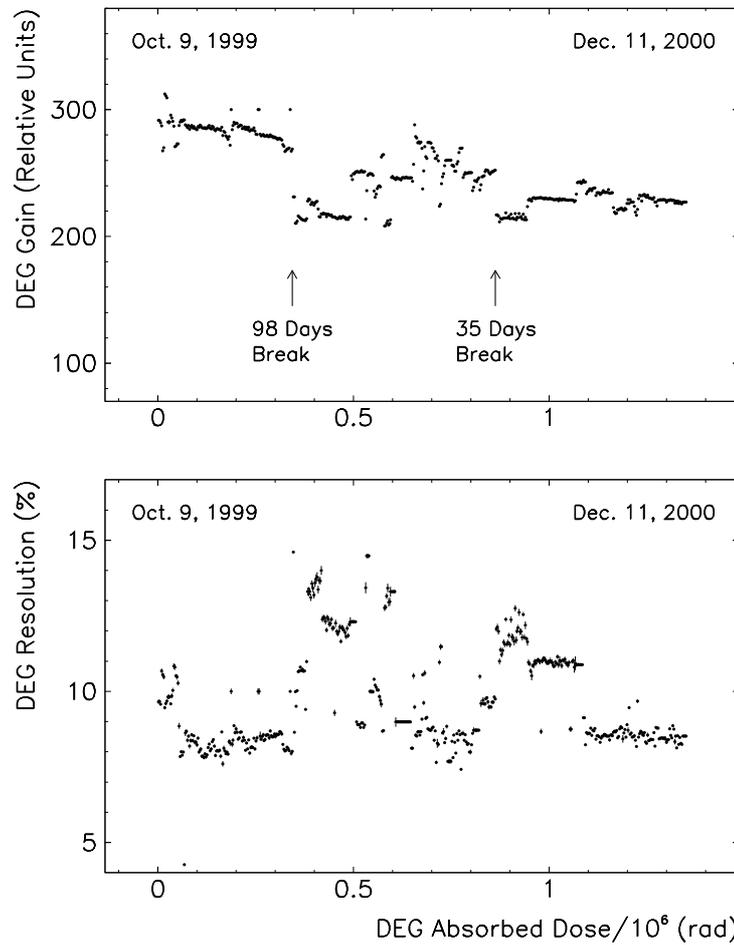
Fig. 5. *Top panel: the gain of the AD counter as a function of the absorbed radiation dose in* Mrad. *Bottom panel: the energy resolution of the active degrader as a function of the cumulative radiation dose in* Mrad.

3.3. Active stopping target (AT)

The PIBETA active target, AT, is a cylindrical plastic scintillator counter 50 mm long with a diameter of 40 mm. The counter is segmented into 9 elements, as shown schematically in Fig. 1b. A 7 mm diam. central cylinder is surrounded by 4 identical tubular segments that compose an inner ring with outer 30 mm diam. The second, outer target ring is made of 4 tubular segments rotated by 45° with respect to the inner ring (cf. Fig. 1b). The 9 pieces are wrapped individually in aluminized Mylar foil isolating them optically from each other. The segments are pressed together and the whole modular assembly is wrapped with black plastic tape. Each

target element is acting as an independent counter, viewed by a miniature (8 mm photo-cathode) Hamamatsu R7400U photomultiplier tube via a 60 mm long, tapered acrylic lightguide.

The uncalibrated deposited energy (ADC) spectrum of the central target segment T_0 recorded with the π-in-beam trigger is depicted in Fig. 6. The events in which the stopping pion deposits its full energy in the target element are clearly distinguished in the high-energy peak. The peak is well described by a Gaussian form with a square-root function tail. The GEANT simulation predicts a peak position at 27.6 MeV, and the average energy deposited in the central target segment T_0 of 16.6 MeV. The events with a stopping particle sharing energy between two or more target segments, due to scattering or to beam divergence, fall into the low energy tail. The same low energy tail is also populated by positrons from delayed weak pion and muon decays.
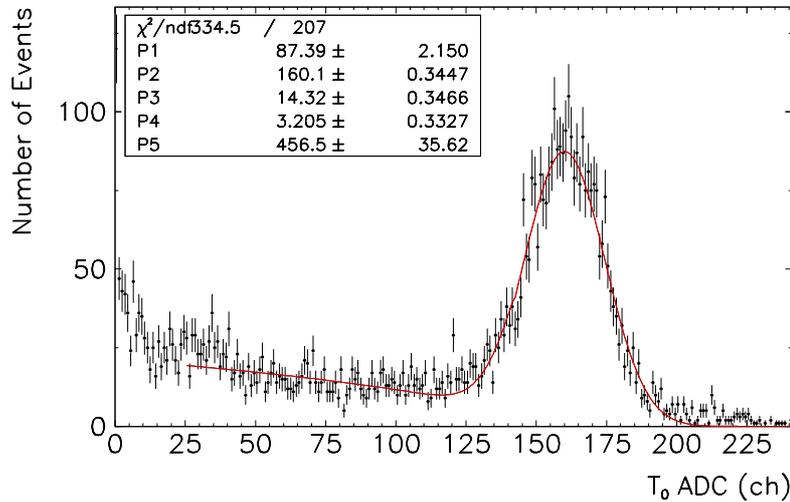

χ^2/ndf	334.5	/ 207
P1	87.39 $\pm$	2.150
P2	160.1 $\pm$	0.3447
P3	14.32 $\pm$	0.3466
P4	3.205 $\pm$	0.3327
P5	456.5 $\pm$	35.62

Fig. 6. Deposited energy spectrum of stopping pions in the central active target segment. Parameters P1–P3 correspond to a Gaussian function, the values P4 and P5 describe a square-root tail function fit.

In Table 1 we give the starting and final gains and resolutions for the three representative target segments. The measured temporal variation in the gain factor and energy resolution of the central target segment over the 15 month period is depicted in Fig. 7. The cumulative absorbed radiation dose is calculated to be 0.5 Mrad. A considerable fall-off in the gain of the T_0 scintillator is evident in the figure: $\simeq 52\%$/Mrad. As in the AD counter, the energy resolution is subject to short-term variations caused by changes in the beam-spot geometry. Over the analyzed period, though, the resolution was degraded by a full 80%. This level of radiation damage makes it necessary to make available identical copies of the AT detector for periodic replacement. The radiation damaged PIBETA target assembly has been replaced annually with new target detectors.
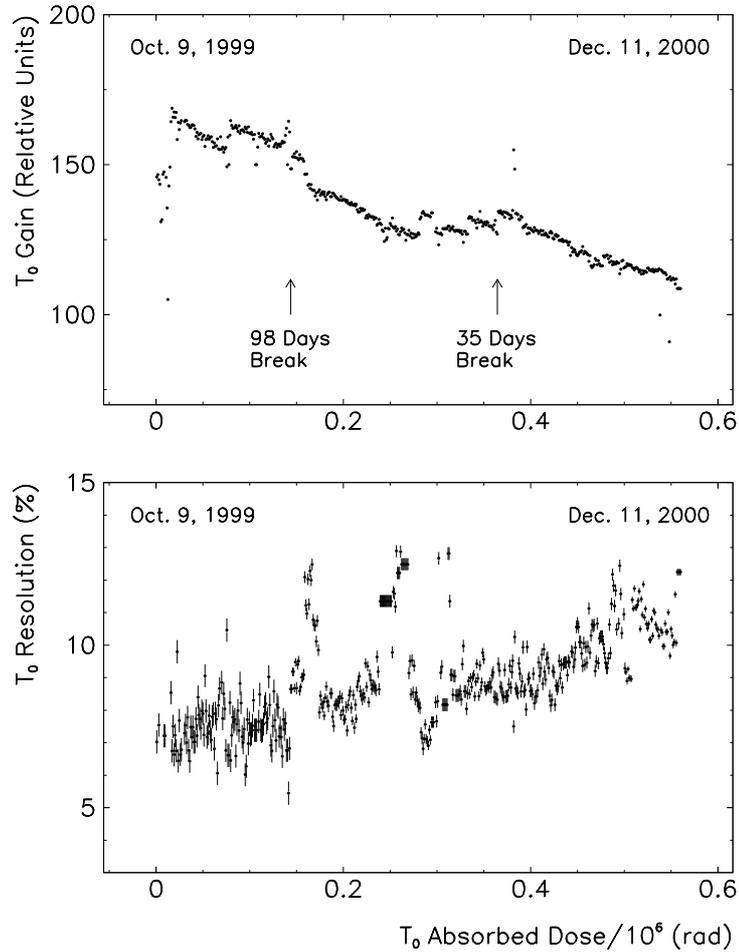
Fig. 7. *Top panel: the gain of AT_0, the central target segment, as a function of the absorbed radiation dose in* Mrad. *Bottom panel: the energy resolution of the AT_0 counter as a function of the cumulative radiation dose in* Mrad.

4. Multiwire Proportional Chambers (MWPCs)

MWPC$_1$ and MWPC$_2$ are a pair of cylindrical multiwire proportional chambers, each with one anode wire plane along the beam direction, and two cathode strip planes in stereoscopic geometry. A general description of the design and operation of the "Dubna"-type cylindrical chambers is given in Ref. [18]. The PIBETA detector cylindrical MWPCs are described in more detail in Refs. [19] and [20]. In this section, we analyze the chamber detection efficiencies measured with minimum ionizing particles.

The detection efficiency ϵ of $MWPC_1$ for minimum ionizing particles (MIPs) can be measured using copious $\mu^+ \rightarrow e^+ \nu \bar{\nu}$ (Michel) positrons emanating from the stopping target,

$$\epsilon_{MWPC_1} = \frac{N(AT \cdot MWPC_1 \cdot MWPC_2 \cdot PV \cdot CsI)}{N(AT \cdot MWPC_2 \cdot PV \cdot CsI)} \,, \qquad (2)$$

where the N's represent the number of Michel events for which all detectors in the parenthesis register coincident hits above their discriminator threshold. The CsI calorimeter signal is discriminated with a low threshold level ($\simeq 5\,MeV$), while a software cut on the PV deposited energy spectrum selects MIP events (Fig. 8). An equivalent expression, obtained by substituting 2 for the index 1, holds for $MWPC_2$. The average MWPC detection efficiencies at the $\simeq 1\,MHz$ π^+ beam stopping rate are $> 95\,\%$ and $> 98\,\%$ for the inner and outer chambers, respectively. Off-line analysis of the individual chamber efficiencies for the period under consideration, which involved $\approx 1.4 \cdot 10^{13}$ (mostly minimum ionizing) particles, found no degradation within the measurement uncertainty (Table 2).
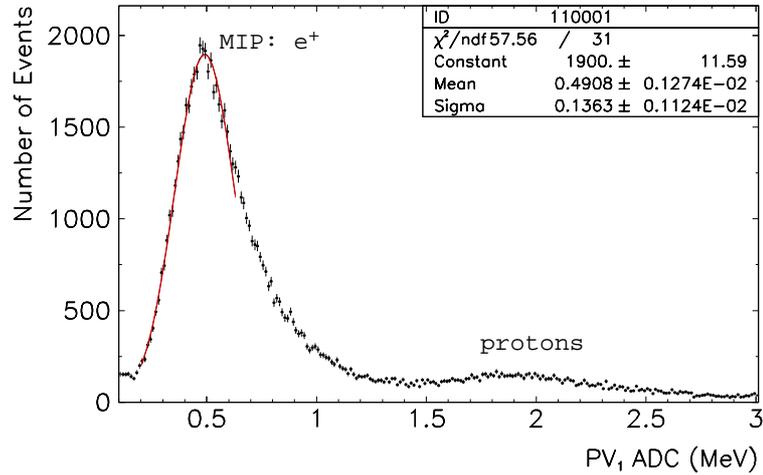

Fig. 8. Calibrated deposited energy (ADC charge) spectrum of minimum-ionizing particles (mostly e^+'s, lower energy peak at $\simeq 0.5\,MeV$) and protons (peak at $\simeq 2.0\,MeV$) in a single representative detector element of the PV hodoscope.

5. Plastic scintillator hodoscope (PV)

The PV (plastic veto) hodoscope is located inside the CsI calorimeter and surrounds the two concentric wire chambers, as shown in Fig. 1. The hodoscope array consists of 20 thin independent plastic scintillator bars that are arranged to form a complete cylinder with a 129 mm radius and a 598 mm long axis that coincides with the beam line and the target axis. The PV hodoscope covers the entire geometrical solid angle subtended by the CsI calorimeter as seen from the target center.

A single PV detector element consists of four main components: (1) thin plastic scintillator bar, (2) two lightguides, one at each end, (3) two photomultiplier tubes, one per lightguide and (4) aluminized Mylar wrapping.

The dimensions of the individual plastic bars made of BC-400 scintillator are $3.18\,\mathrm{mm} \times 41.9\,\mathrm{mm} \times 598\,\mathrm{mm}$. Each thin plastic scintillator bar, along with the attached lightguides, is wrapped in $0.25\,\mu\mathrm{m}$ thick aluminized Mylar foil to optically separate it from the adjacent bars, and to provide a reflective surface that increases the amount of light reaching the phototubes. Scintillation light is viewed by two Burle Industries S83062E photomultiplier tubes, one on each end. These tubes are $28\,\mathrm{mm}$ diam. head-on fast PMTs with 10 stages.

The hodoscope array is supported from the inside by a $530\,\mathrm{mm}$ long carbon-fiber cylinder with a total thickness of $1\,\mathrm{mm}$, corresponding to $5.3 \cdot 10^{-3}$ radiation lengths. The hodoscope modules are kept tight around the support cylinder by a helix-wound, thin plastic string tensioned at the extreme ends of the detector stand.

The PV charged particle detection efficiency is evaluated separately for minimum-ionizing positrons with total energy above $5\,\mathrm{MeV}$ and for non-relativistic protons with kinetic energy in the range $10 - 150\,\mathrm{MeV}$. Fig. 8 shows the measured energy spectrum of positrons and protons in the PV detector, corrected for the angle of incidence.

At the nominal π^+ stopping rate, the individual plastic scintillator phototubes are counting at the rate of $\approx 130\,\mathrm{kHz}$, while the entire PV hodoscope is taking $\approx 0.88\,\mathrm{MHz}$. The total radiation dose absorbed by the PV hodoscope array throughout the analyzed period is $40\,\mathrm{krad}$.

A charged particle track is defined by the coincident hits in the active target, AT, two wire chambers, MWPC_1 and MWPC_2, and the CsI calorimeter, CsI. The PV detection efficiency is defined as the following ratio

$$\epsilon_{\mathrm{PV}} = \frac{N(\mathrm{AT} \cdot \mathrm{MWPC}_1 \cdot \mathrm{MWPC}_2 \cdot \mathrm{PV} \cdot \mathrm{CsI})}{\mathrm{N}(\mathrm{AT} \cdot \mathrm{MWPC}_1 \cdot \mathrm{MWPC}_2 \cdot \mathrm{CsI})} \ , \tag{3}$$

where each N represents the number of events satisfying the condition in the parenthesis. The average PV detection efficiency measured during the detector commissioning period was $\epsilon_{\mathrm{PV}} \geq 99.0\,\%$ (Table 2). No significant long-term change in the PV detection efficiency was observed.

As for the previously discussed detectors, Table 1 lists the starting and final gains and resolutions for two representative PV detectors. The temporal dependence of the detector light output for PV bar number 1 is shown in Fig. 9. Its gain factor dropped by $0.25\%/\mathrm{krad}$, giving a cumulative degradation over the production period of 10%. The energy resolution on the other hand shows a barely measurable change.

By combining the information from the PV hodoscope and the MWPC pair, the charged-particle tracking system achieves an overall MIP detection inefficiency in the range $(1.0 \pm 0.2) \cdot 10^{-5}$, while operating in the environment of $\approx 1\,\mathrm{MHz}$ stopped π^+'s in the target.
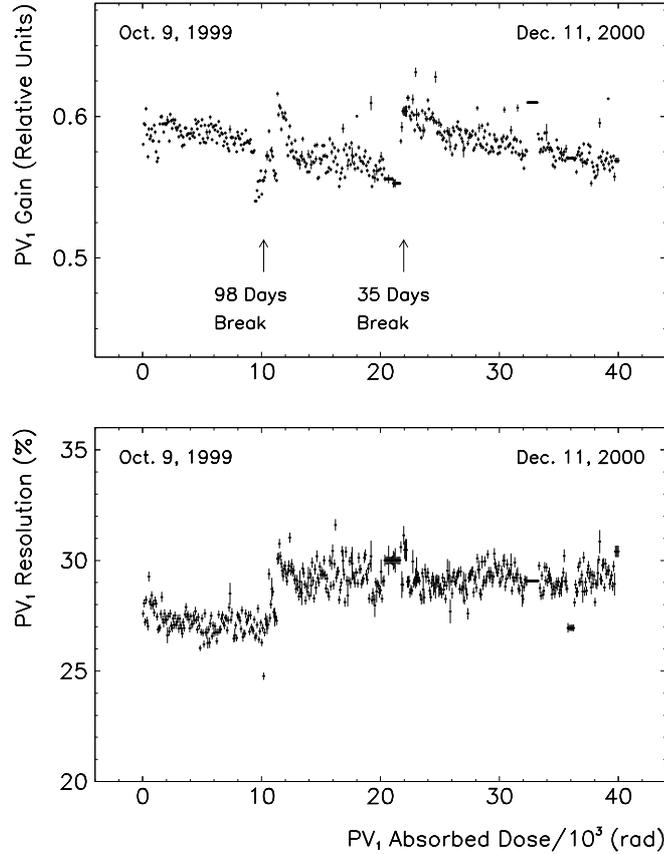
Fig. 9. Top panel: the gain of the PV counter number 1 as a function of the absorbed radiation dose in krad. *Bottom panel: fractional energy resolution of the forward PV counter number 1 as a function of the cumulative radiation dose in* krad. *The discontinuity in the fractional resolution plot around 10* krad *is related to a servicing operation.*

6. *Pure* CsI *calorimeter modules*

The shower calorimeter lies at the heart of the PIBETA detector. Pure (undoped) CsI single crystal (Refs. [21],[22] and [23]) was chosen as the calorimeter material.

The PIBETA calorimeter consists of 240 pure CsI crystals. Spherical geometry is obtained by the ten-frequency class II geodesic triangulation of an icosahedron [24]. The chosen geodesic division results in 220 hexagonal and pentagonal truncated pyramids covering a total solid angle of $0.77 \times 4\pi$ sr. Additional 20 crystals surround two detector openings for the beam entry and detector access and act as electromagnetic shower leakage vetoes. The inner radius of the crystal ball

is 260 mm, and the axial module length is 220 mm, corresponding to 12 radiation lengths, as $X_0(\text{CsI}) = 18.5$ mm [25].

There are nine different detector module shapes: four irregular hexagonal truncated pyramids (labeled Hex-A, Hex-B, Hex-C and Hex-D), one regular pentagonal (Pent) and two irregular half-hexagonal truncated pyramids (Hex-D1 and Hex-D2), plus two trapezohedrons which function as calorimeter vetoes (Vet-1 and Vet-2). The volumes of the PIBETA CsI detector modules vary from 797 cm^3 (Hex-D1/2) to 1718 cm^3 (Hex-C).

The first 25 PIBETA crystals were manufactured in the Bicron Corporation facility in Newbury, Ohio [17]. The remaining 215 CsI scintillators were grown in the Institute for Single Crystals in Harkov (AMCRYS), Ukraine. Preliminary quality control, including the optical and mechanical crystal properties, was performed at the production sites.

After completing physical measurements, all crystal surfaces were hand-polished with a mixture of $0.2\,\mu$m aluminum oxide powder and etylenglycol. The surfaces of each CsI crystal were then painted with a special organo-silicon mixture. The wavelength-shifting lacquer developed by the Harkov Single Crystals Research Institute [26] provides an optical treatment of crystal surfaces superior to more common matting or wrapping treatments. The lacquer contains a wavelength-shifting ladder organosilicon copolymer with the chemical composition PPO+POPOP+COUM.1, where PPO is 2.5–Diphenyloxazole, POPOP represents 1.4-Di-2-(5-Phenyloxazolile-Benzene) and COUM.1 is 7-Diethylamine-4-Methylcoumarin [27].

EMI 9822QKB 10-stage fast photomultipliers [28] with 75 mm diam. end windows are attached to the back faces of hexagonal and pentagonal CsI crystals using a 300 μm layer of silicone Sylgard 184 elastomer (Dow Corning RTV silicone rubber plus catalyst). The resulting crystal–photomultiplier tube couplings are strong and permanent, but can be broken by application of a substantial tangential force. Smaller half-hexagonal and trapezial detector modules are equipped with 46 mm diam. 10-stage EMI 9211QKA phototubes [28]. Both photocathodes have quartz windows transmitting photons down to 175 nm. The window transparency, peaking at $\approx$ 380 nm [28], is approximately matched to the spectral excitation of a pure CsI fast scintillation light component with a peak emission at $\approx$ 310 nm at room temperature [29].

Calibrated energy spectra of the calorimeter detector show that the individual modules receive between 5 and 10 MeV energy depositions in a large sample of events averaged over all physics triggers. The accumulated radiation doses for individual CsI counters have been between 40 rad and 160 rad (see Table 1).

A deposited energy (ADC) spectrum, calibrated in MeV and representing a sum of ADC values for one CsI detector and its nearest neighbors, is shown as an example in Fig. 10. The event trigger is a high threshold ($\simeq$ 52 MeV) delayed π^+ gate trigger that preferentially selects both $\mu \to e\nu\bar{\nu}$ positrons which have a continuous energy spectrum with a 52.5 MeV endpoint, and the monoenergetic 70 MeV $\pi \to e\nu$ positrons. The μ decay positron spectrum is clipped on the left very near its endpoint by the $\simeq$ 52 MeV trigger discriminator threshold. The monoenergetic π

decay positron line is used for the automatic, computer-controlled gain matching of the individual CsI detectors.
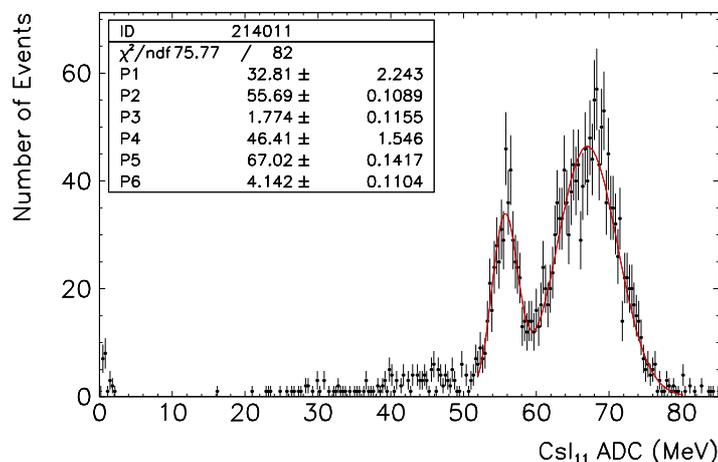

ID	214011	
χ^2/ndf 75.77	/	82
P1	32.81 ±	2.243
P2	55.69 ±	0.1089
P3	1.774 ±	0.1155
P4	46.41 ±	1.546
P5	67.02 ±	0.1417
P6	4.142 ±	0.1104

Fig. 10. *Calibrated energy spectrum of a single* CsI *detector (CsI HEX-A module S011, 10 runs). The higher energy peak at* ~ 68 MeV *represents monoenergetic* $\pi^+ \to e^+ \nu$ *positrons, the lower part of the spectrum is populated by* $\mu^+ \to e^+ \nu \bar{\nu}$ *Michel positrons cut by a* ~ 52 MeV *trigger discriminator threshold.*
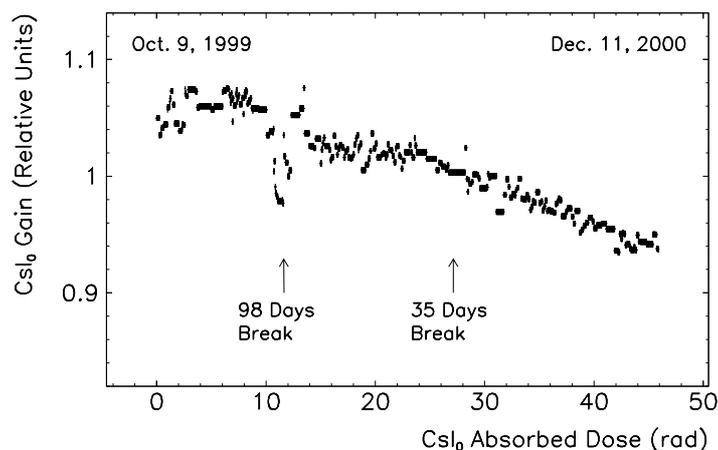

Fig. 11. *Normalized gain of the* CsI *detector number 0 (Bicron pentagon module) as a function of the absorbed radiation dose in* rad.

Because both the software gain factors and the PMT high voltages of all CsI counters are varied after each run, the relevant real gain factors are defined by Eq. (1). Representative gain variations for three different CsI detectors are shown in Figs. 11 to 13. These measurements show different gain degradation rates of up to $\geq 40\,\%/(100\,\text{rad})$. An increase in gain following extended beam breaks is a common feature of the CsI light response, as seen in the three figures.
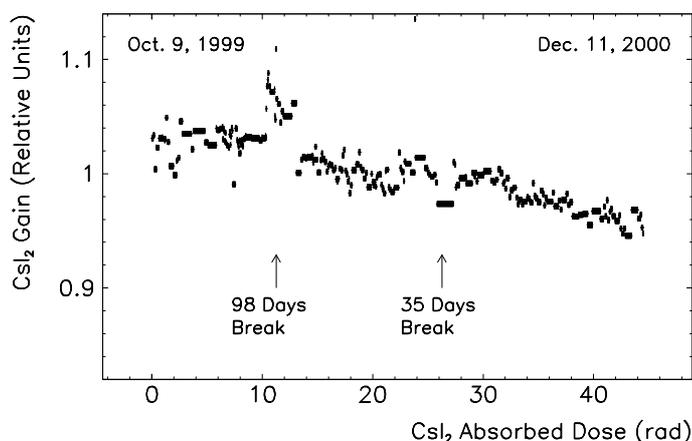
Fig. 12. Normalized gain of the CsI detector number 2 (Harkov pentagon module) as a function of the absorbed radiation dose in rad.
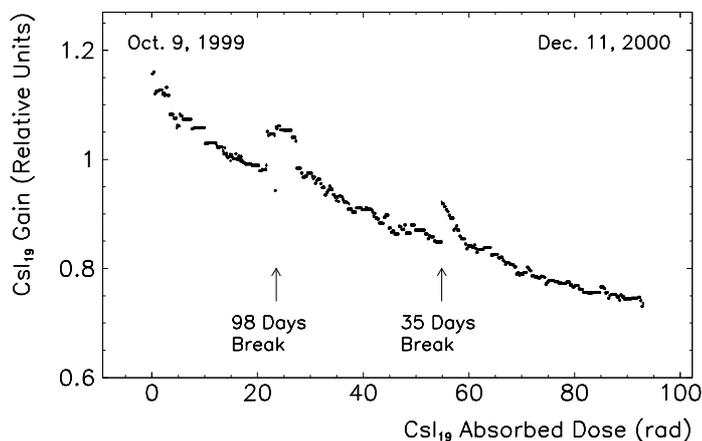

Fig. 13. Normalized gain factor of the CsI detector number 19 (Harkov HEX-A module) as a function of the absorbed radiation dose in rad.

The overall CsI calorimeter gain and energy resolution are determined from the calibrated experimental energy spectra of all 240 CsI detectors. The results are summarized in Table 1. As it accumulated an average radiation dose of 119 rad, the PIBETA calorimeter gain decreased 17 % and the overall energy resolution was lowered between 5.5% and 6.0%. This decrease, however, should not be attributed entirely to radiation damage, as the crystals were subject to other sources of performance degradation over time, such as absorption of humidity on the crystal surfaces, slow plastic deformation of individual modules under pressure (CsI is highly malleable, while the detectors are self-supporting, with the entire weight of over 1 ton distributed among the elements). Thus, the above performance degradation provides a very loose upper limit on the radiation effects on pure CsI.

7. Conclusions

We have analyzed the temporal changes in gains, energy resolutions and detection efficiencies of the active elements of the PIBETA detector during 15 month period of production data taking. We find measurable decreases in energy gains and degradations in energy resolutions, in particular for the beam detectors that were exposed to high radiation doses as well as for more radiation-sensitive pure CsI calorimeter modules. These changes in the detector responses are monitored online throughout the production running and documented in the replay data analysis. The changes affect the energy calibration of the PIBETA detector elements and have to be properly taken into account when defining the software energy cuts in the physics analysis of rare pion and muon decays.

Acknowledgements

References

[1] D. Počanić et al., *A Proposal for a Precise Measurement of the $\pi^+ \to \pi^0 e^+ \nu$ Decay Rate*, PSI R-89.01, Paul Scherrer Institute, Villigen, 1991.

[2] G. Marini, I. Donatelli, A. Nigro, G. Martellotti, M. De Vincenzi, A. Sciubba, F. Coninckx, G. Crosetti, and H. Schönbacher, *Radiation Damage to Organic Scintillation Materials*, CERN Yellow Report 85-08 (CERN, Geneva, 1985).

[3] A. D. Bross and A. Pla-Dalmau, *Radiation-Induced Hidden Absorption Affects in Polystyrene-Base Plastic Scintillator*, FERMILAB-Pub-90/224 (FERMILAB, Batavia, 1990).

[4] B. Bicken, U. Holm, T. Marckmann, K. Wick, and M. Rohde, IEEE Trans. Nucl. Sci. **NS-38** (1991) 188.

[5] RADECS 93 Conference Proceedings, IEEE Trans. Nucl. Sci. **NS-41** (1994) 421.

[6] RADECS 95 Conference Proceedings, IEEE Trans. Nucl. Sci. **NS-43** (1996) 769.

[7] V. G. Senchishin, F. Markley, V. N. Lebedev, V. E. Kovtun, V. S. Koba, A. V. Kuznichenko, V. D. Tizkaja, J. A. Budagov, G. Bellettini, V. P. Seminozhenko, I. I. Zalubovsky, and I. E. Chirikov-Zorin, Nucl. Instrum. Meth. A **364** (1995) 253.

[8] M. L. Andrieux, *Review of Radiation Tests on Opto-Electronic Components and Material for LHC*, accessible at `http://isnwww.in2p3.fr/atlas/andrieux/radpbn.html`.

[9] M. Kobayashi, M. Ieiri, K. Kondo, T. Miura, H. Noumi, M. Numajiri, Y. Oki, T. Suzuki, M. Takasaki, K. Tanaka, Y. Yamanoi, S. Sugimoto, and M. Ishii, *Crystal 2000: Proceedings of Int. Workshop on Heavy Scintillators for Scientific and Industrial Applications*, Chamonix, France (1992), p. 513.

[10] A. Roodman, *Crystal 2000: Proceedings of Int. Workshop on Heavy Scintillators for Scientific and Industrial Applications*, Chamonix, France (1992) p. 479.

[11] C. L. Woody, J. A. Kierstead, P. W. Levy, and S. Stoll, IEEE Trans. Nucl. Sci. **NS-39** (1992) 524.

[12] G. Eigen, and D. G. Hitlin, *Crystal 2000: Proceedings of Int. Workshop on Heavy Scintillators for Scientific and Industrial Applications*, Chamonix, France (1992) p. 467.

[13] M. Kobayashi, M. Ieiri, K. Kondo, T. Miura, H. Noumi, M. Numajiri, Y. Oki, T. Suzuki, M. Takasaki, K. Tanaka, Y. Yamanoi, S. Sugimoto, and M. Ishii, Nucl. Instrum. Meth. A **328** (1993) 501.

[14] *PSI Users' Guide: Accelerators Facilities*, Paul Scherrer Institute, Villigen PSI (1994).

[15] R. Brun, F. Bruyant, M. Maire, A. C. McPherson and P. Zanarini, *GEANT3.21 DD/EE/94-1*, CERN, Geneva (1994).

[16] W. R. Leo, *Techniques for Nuclear and Particle Physics Experiments*, Springer-Verlag, Berlin (1987).

[17] *Bicron Corporation Catalog*, Bicron Corporation, Newbury (1989), and online at URL `http://www.crismatec.com/`.

[18] N. P. Kravchuk, Phys. Particles Nuclei **25** (1994) 1244.

[19] V. V. Karpukhin, I. V. Kisel, A. S. Korenchenko, S. M. Korenchenko, N. P. Kravchuk, N. A. Kuchinsky, N. V. Khomutov, and S. Ritt, Nucl. Instrum. Meth. A **418** (1998) 306.

[20] V. V. Karpukhin, I. V. Kisel, A. S. Korenchenko, S. M. Korenchenko, N. P. Kravchuk, N. A. Kuchinsky, N. V. Khomutov, and S. Ritt, Instrum. Exp. Tech. **42** (1999) 335.

[21] H. Kobayashi, A. Konaka, K. Miyake, T. T. Nakamura, T. Nomura, N. Sasao, T. Ya-mashita, S. Sakuragi and S. Hashimoto, Kyoto University Preprint KUNS-900 (1987).

[22] S. Kubota, H. Murakami, J. Z. Ruan, N. Iwasa, S. Sakuragi, and S. Hashimoto, Nucl. Inst. and Meth. A **273** (1988) 645.

[23] S. Kubota, S. Sakuragi, S. Hashimoto and J. Z. Ruan, Nucl. Inst. and Meth. A **268** (1988) 275.

[24] H. Kenner, *Geodesic Math and How to Use it*, University of California Press, Berkeley (1976).

[25] *Review of Particle Physics*, Phys. Rev. D **66** (2002) 01001; Latest `WWW` update accessible at `http://www-pdg.lbl.gov`.

[26] V. I. Goriletsky, L. A. Andryuschenko and A. M. Kudin, private communication, Alkali Halide Crystal Division, Institute for Single Crystals, National Academy of Sciences of Ukraine, 60 Lenin Prosp., 310001 Harkov, Ukraine.

[27] D. R. Lide, *CRC Handbook of Chemistry and Physics*, 71st ed., p. 3-357, CRC Press, Boca Raton (1990).

[28] *THORN-EMI Electron Tubes Catalog, Photomultipliers and Accessories*, Rockaway, NJ (1993).

[29] C. L. Woody, P. W. Levy, J. A. Kierstead, T. Skwarnicki, Z. Sobolewski, M. Goldberg, N. Horwitz, P. Souder and D. F. Anderson, IEEE Trans. Nucl. Sci., **NS-37** (1990) 492.

OTPORNOST NA ZRAČENJE DIJELOVA DETEKTORA PIBETA

Ispitivali smo trajne promjene amplitude, energijskog razlučivanja i učinkovitosti detekcije aktivnih dijelova detektorskog sustava PIBETA. Plastični scintilacijski detektori koji definiraju snop ozračeni su do 2 Mrad. Par višežičanih proporcionalnih komora i tanak valjak plastičnih scintilacijskih detektora ozračeni su do 40 krad. CsI kalorimetrijski detektori ozračeni su do 120 rad.